

Testing the Kibble-Zurek Mechanism through a Digital Quantum Computer

Santiago Higuera-Quintero^{1,*}, Ferney J. Rodríguez^{1,†}, Luis Quiroga^{1,‡} and Fernando J. Gómez-Ruiz^{2,§}

¹*Departamento de Física, Universidad de los Andes, A.A. 4976, Bogotá D. C., Colombia*
²*Instituto de Física Fundamental IFF-CSIC, Calle Serrano 113b, Madrid 28006, Spain*

The Kibble-Zurek mechanism (KZM) captures the essential physics of nonequilibrium quantum phase transitions with symmetry breaking. KZM predicts an universal scaling power law for the defect density which is fully determined by the system's critical exponents at equilibrium and the quenching rate. In this work, we numerically tested the KZM predictions for the simplest quantum case, a single qubit under the Landau-Zener evolution, on an open access IBM quantum computer (IBM-Q). We report on extensive IBM-Q experiments on individual qubits embedded in different circuit environments and topologies, separately elucidating the role of qubit degree of isolation and the increasing decoherence effects associated with the quantum circuit depth. Our results confirm that the increasing of the circuit depth acts as a decoherence source, producing a rapid depart of the experiment data from the theoretical unitary prediction, since the gates errors accumulate.

I. INTRODUCTION

Characterizing the non-equilibrium dynamics in noisy intermediate-scale quantum (NISQ) devices plays an important role in developing both hardware and architecture designs in the search for scalable quantum computers. NISQ devices have recently attracted tremendous interest, resulting in rapid progress in fundamental studies of novel hardware and architecture together with promising potential for quantum computing [1, 2]. The advance in the development of NISQ devices demonstrated a “quantum advantage” in solving sampling problems [3–5]. To further improve quantum advantage, it is desirable that the devices show important features such as high-fidelity gates, qubits with long coherence times, control of state preparation, and measurement. [6–8]. Recently, open-access/online NISQ devices, such as those provided by the IBM Quantum Experience (IBM-Q) platform which is publicly available on the internet [9], have become available showing significant improvements along the last few years. Although, they still suffer from noise and scalability limitations, they do offer the unique possibility of experimenting with actual few qubit quantum devices which gives us the opportunity of carrying out a rigorous study of dynamical quantum properties in different settings along the real time-dynamics of quantum hardware.

A key feature of merit in the current NISQ regime is the ability to simulate non-equilibrium quantum dynamics. A prominent paradigm to unravel signatures of universal dynamics is the Kibble-Zurek mechanism (KZM) [10–13]. In the scenario of a finite-rate spontaneous symmetry breaking, the KZM predicts the production of topological defects (kinks, vortices,

strings) or in general non-equilibrium excitations (in both short- and large-ranged interacting systems) in the course of either quantum [14–16] or classical [11, 12] phase transitions. The key result of KZM is concerned with the fact that the mean value of density of the topological defects scales as a power law of the quench rate. Furthermore, new evidence of scaling in the high-order cumulants has also been recently shown [17, 18]. These theoretical predictions have been observed in various experimental platforms such as Bose Gas [19], trapped ions [20], quantum annealer [21, 22], Bose-Einstein Condensate [23], Rydberg atoms [24]. In 2005, Damski established a close relationship between second order quantum phase transitions and avoided level crossing evolutions. Thus, the Landau-Zener (LZ) model [25–28] sets itself up as the simplest paradigmatic scenario for probing KZM [29, 30]. This relationship has been probed by using optical interferometer [31], superconducting qubit [32, 33], and ion trapped [34].

IBM-Q currently access up to 5-qubit machines based on superconducting transmon qubits, using *Qiskit* open-source software [35, 36]. Those machines has been successfully utilized in simulating spin models [37, 38], topological fermionic models [39], quantum entanglement [40–44], far-from-equilibrium dynamics [45], non-equilibrium quantum thermodynamics [46, 47], open-quantum systems [48], among others. In this work, we test the KZM on the simplest, but important case of a single qubit (LZ model), through experiments on the Qiskit [35] simulator and real quantum hardware, and taking into account the limits required to obtain accurate results in each case. We successfully reproduced the LZ dynamics under a discrete time evolution. Noticeable effects of decoherence are observed and explained by a simple phenomenological model of relaxation and dephasing for an open quantum system. Furthermore, analysis and estimation of the experimental asymptotic probability allows us to verify the universal KZM in a timescale appropriate for an almost closed system under quench regime.

* s.higuera@uniandes.edu.co

† frodrigu@uniandes.edu.co

‡ lquiroga@uniandes.edu.co

§ fernandojavier.gomez@iff.csic.es

This paper is organized as follows. A brief review on KZM, the LZ model and its close connection with KZM, are presented in Sect. II. In Sect. III we present the experimental platform. The contrast between the theoretical and experimental results is collected in Sect. IV. Finally, we summarize the main conclusions in Sect. V.

II. THEORETICAL BACKGROUND

A. The Kibble-Zurek Mechanism

The KZM describes the dynamics of a system across a continuous symmetry breaking second-order phase transition induced by the change of a control parameter λ . When the system is driven through the critical point λ_c , both the correlation length ξ and the relaxation time τ diverges as:

$$\xi = \xi_0 |\epsilon|^{-\nu}, \quad \tau = \tau_0 |\epsilon|^{-z\nu}. \quad (1)$$

where, $\epsilon = (\lambda - \lambda_c)/\lambda$ marks the separation from the critical point. The spatial and dynamic *equilibrium* critical exponents are given by ν and z , respectively, while the mesoscopic behavior of the system is contained in the dimensional constants ξ_0 and τ_0 . If the quench varies linearly in time, $\epsilon(t) = t/t_a$, where t_a denotes a quench or annealing time scale, the system reaching the critical point at $t = 0$. Therefore, the equilibrium effective relaxation time diverges as Eq. (1). This phenomenon known as critical slowing down can be used to describe the time evolution across a phase transition as a sequence of three stages. Initially, the system is prepared in the high symmetry phase from which it evolves within an adiabatic evolution stage. Secondly, the evolution enters in an impulse stage in the neighborhood of the phase transition where the system is effectively frozen. Finally, when the system is far away from the critical point, the dynamics is adiabatic again. These three regimes are schematically represented in Fig. 1(a). The three regions are separated by two points marked as $-\hat{t}_{\text{KZM}}$ and \hat{t}_{KZM} , in such a way that the freeze-out occurs at the instant $\hat{t}_{\text{KZM}} \sim (\tau_0 t_a^{z\nu})^{1/(1+z\nu)}$. The main point of the KZM argument is that the size average or correlation length, $\hat{\xi}$, of the domains in the broken symmetry phase is set by the equilibrium correlation length evaluated at the freeze-out time. Therefore, the density of excitations, resulting from the quench evolution, scales as $d \sim \hat{\xi}^{-D}$ where D is the dimensionality of the system goes as:

$$d_{\text{KZM}} \sim \frac{1}{\xi_0} \left(\frac{\tau_0}{\tau_Q} \right)^{\frac{D\nu}{1+z\nu}}. \quad (2)$$

This result was initially derived in the classical domain [11, 12] and subsequently extended to quantum systems [14, 15]. Additionally, The KZM has also been extended to novel scenarios including long-range interactions [16, 49, 50], inhomogeneous systems [51–53], and nonlinear quenches [54, 55].

B. Landau-Zener model

Consider a two-level system, with gap Δ , described by the time-dependent Hamiltonian ($\hbar = 1$):

$$\hat{H}(t) = -\frac{\varepsilon(t)}{2} \hat{\sigma}_z - \frac{\Delta}{2} \hat{\sigma}_x. \quad (3)$$

With $\hat{\sigma}_n$ the Pauli matrix along $n \in \{x, y\}$ direction. We define the *adiabatic* states as the Hamiltonian eigenvectors at $\Delta = 0$ and consequently eigenvectors for the Pauli operator $\hat{\sigma}_z$: $\hat{\sigma}_z |0\rangle = +1|0\rangle$ and $\hat{\sigma}_z |1\rangle = -1|1\rangle$. The respective (adiabatic) energy levels are $E_{0,1} = \mp \varepsilon(t)/2$. Now, the adiabatic instantaneous eigenvalues $E_{\pm}(t)$ and eigenstates $|E_{\pm}(t)\rangle$ are solutions of $\hat{H}(t)|E_{\pm}(t)\rangle = E_{\pm}(t)|E_{\pm}(t)\rangle$. The instantaneous gap energy is given by $\Delta E = E_+ - E_- = \sqrt{\varepsilon^2(t) + \Delta^2}$. In the main panel of Fig. 1(b), we depicted the inverse of the energy gap as a function of time while the instantaneous adiabatic eigenvalues are shown as an inset in the Fig 1(b). The eigenstates are written as a linear combination of the diabatic states as $|\psi(t)\rangle = \alpha(t)|0\rangle + \beta(t)|1\rangle$. By solving the corresponding eigenequation in terms of parabolic cylinder functions $\mathbf{D}_p(z)$, and using the substitution $z = t \exp[i\pi/4]/\sqrt{t_a}$, we obtain the transition amplitudes as:

$$\begin{aligned} \alpha(z) &= \frac{e^{-i\frac{3\pi}{4}}}{\sqrt{\delta}} [\delta \chi_1 \mathbf{D}_{-1-i\delta}(z) + \chi_2 \mathbf{D}_{i\delta}(iz)], \\ \beta(z) &= \chi_1 \mathbf{D}_{-i\delta}(z) + \chi_2 \mathbf{D}_{-1+i\delta}(iz). \end{aligned} \quad (4)$$

where $\delta = \Delta^2 t_a/4$ is the adiabaticity parameter. Moreover, χ_1 and χ_2 are found from the initial condition at

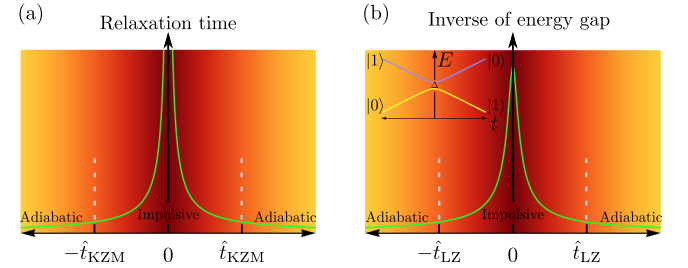


Figure 1. **Connection between KZM and avoided level crossing in a LZ transition.** (a) In a continuous second order phase transition, the relaxation time diverges near the critical point. The KZM approximation takes into account the total dynamics divided in three stages (adiabatic, impulsive, and adiabatic) represented by the graduated yellow-dark red-yellow colors and separated by the freeze out-time \hat{t}_{KZM} . (b) The inverse of the energy gap in LZ exhibits a similar behavior of the relaxation time. However, it is not divergent at the crossing point. By similar analogy, we divided the LZ dynamics in the same three KZM regimes and separated by the Landau-Zener jump time \hat{t}_{LZ} . Inset: Avoided level crossing LZ.

$z = z_i$ (see Appendix A):

$$\begin{aligned}\chi_1 &= \frac{e^{i\frac{3\pi}{4}}\sqrt{\delta}\mathbf{D}_{-1+i\delta}(iz_i)\alpha(z_i) - \mathbf{D}_{i\delta}(iz_i)\beta(z_i)}{\delta\mathbf{D}_{-1-i\delta}(z_i)\mathbf{D}_{-1+i\delta}(iz_i) - \mathbf{D}_{-i\delta}(z_i)\mathbf{D}_{i\delta}(iz_i)}, \\ \chi_2 &= \frac{-e^{i\frac{3\pi}{4}}\sqrt{\delta}\mathbf{D}_{-i\delta}(z_i)\alpha(z_i) + \delta\mathbf{D}_{-1-i\delta}(z_i)\beta(z_i)}{\delta\mathbf{D}_{-1-i\delta}(z_i)\mathbf{D}_{-1+i\delta}(iz_i) - \mathbf{D}_{-i\delta}(z_i)\mathbf{D}_{i\delta}(iz_i)}.\end{aligned}\quad (5)$$

Notice that, Eqs. (4) and (5) are valid for any arbitrary initial condition and final time t . For the experimental implementation, we discuss below, we are interested in studying the system's evolution from an initial state starting in the anticrossing point at $t = 0$. (In the Appendix A 1, the formal solutions for this particular initial condition is summarized).

C. Connection between the KZM and LZ evolution

Following the seminal arguments exposed in Ref. [29, 30], we divided the dynamics through the anti-crossing into three stages similarly to KZM adiabatic-impulsive-adiabatic scenario. Without loss of generalization, we assume that the system starts at $t_i \rightarrow -\infty$ from the ground state $|E_-\rangle$, and then it evolves to $t_f \rightarrow \infty$. We define a natural time scale given by the inverse of the energy gap:

$$\frac{1}{E_+(\hat{t}_{\text{LZ}}) - E_-(\hat{t}_{\text{LZ}})} = \eta\hat{t}_{\text{LZ}}. \quad (6)$$

where, $E_{\pm}(t)$ are the adiabatic energy eigenvalues at time $t = \hat{t}_{\text{LZ}}$ and η is a constant. Using Eq. (3), we obtained

$$\frac{\hat{t}_{\text{LZ}}}{t_a} = \frac{\Delta}{\sqrt{2}} \sqrt{\sqrt{1 + \frac{4}{(\Delta^2\eta t_a)^2}} - 1}. \quad (7)$$

The adiabatic-impulsive-adiabatic approximation assumes that the evolution wave function $|\psi(t)\rangle$ of the system satisfies:

- Adiabatic dynamics: from $t_i = -\infty$ to $t = -\hat{t}_{\text{LZ}}$

$$|\psi(t)\rangle \approx e^{i\Phi_1} |E_-(t)\rangle.$$

- Impulsive dynamics: from $t = -\hat{t}_{\text{LZ}}$ to $t = \hat{t}_{\text{LZ}}$

$$|\psi(t)\rangle \approx e^{i\Phi_2} |E_-(-\hat{t}_{\text{LZ}})\rangle.$$

- Adiabatic dynamics: from $t = \hat{t}_{\text{LZ}}$ to $t_f = \infty$

$$|\langle\psi(t)|E_-(t)\rangle|^2 \approx A.$$

Where Φ_1, Φ_2 are global phases, and A is a constant. Following the adiabatic-impulsive-adiabatic (AI) approximation, Damski in Refs. [29, 30] reported the probability of finding the LZ system in the excited state at $t_f \gg t_{\text{LZ}}$, a calculation we briefly summarize for the

sake of completeness in view of our main experimental interest.

From now on, we focus on the LZ dynamics for the evolution starting at the anticrossing point. The initial state at $t = 0$ is then expressed as $|E_-(0)\rangle = (|1\rangle - |0\rangle)/\sqrt{2}$, and consequently the transition probability $P_{\text{AI}} = |\langle E_+(\hat{t}_{\text{LZ}}) | E_-(0)\rangle|^2$ is given by [29, 30]:

$$\begin{aligned}P_{\text{AI}} &= \frac{1}{2} \left(1 - \frac{1}{\sqrt{1 + \hat{\varepsilon}^2}} \right), \\ &= \frac{1}{2} - \frac{1}{2} \sqrt{1 - \frac{2}{(\eta t_a)^2 + \eta t_a \sqrt{(\eta t_a)^2 + 4} + 2}}.\end{aligned}\quad (8)$$

We fixed the two-level system gap $\Delta = 1$. Additionally, $\hat{\varepsilon} = \varepsilon(\hat{t}_{\text{LZ}})$ is the linear bias at time $t = \hat{t}_{\text{LZ}}$. Expanding Eq. (8) into a series of $\sqrt{t_a}$, we obtained:

$$P_{\text{AI}} = \frac{1}{2} - \frac{\sqrt{\eta}}{4} t_a^{1/2} + \frac{\eta\sqrt{\eta}}{8} t_a^{3/2} + \mathcal{O}(t_a^{5/2}). \quad (9)$$

which will be relevant for testing the predictions of the universal KZM adiabatic-impulsive approximation below.

III. EXPERIMENTAL IBM-Q PLATFORM

IBM-Q devices are equipped with a finite and complete set of basis gates on which any quantum

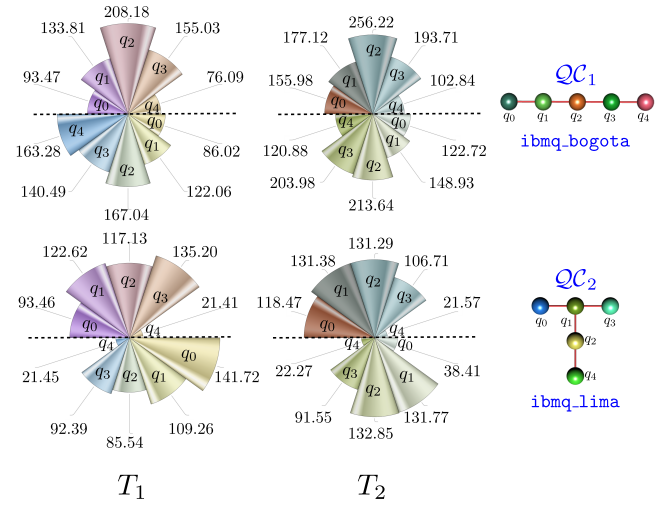


Figure 2. **Decoherence times in different IBM-Q Experimental platforms.** In the like-pie chart, we contrast the thermal relaxation time (T_1) and dephasing time (T_2), in (μs) , for two different topology circuits, simply called \mathcal{QC}_1 and \mathcal{QC}_2 (see text for details). Due to in situ IBM machine calibration routines the times T_1 and T_2 may change. Every like-pie chart is divided in two sectors by a dashed line, where the upper and lower sectors corresponding to decoherence times at two different dates.

circuit must be decomposed into. We implemented our experimental studies in two topologies or processors types. Figure 2 show the device layout for the IBMQ 5-qubit `ibmq_bogota` (Falcon r5.11L topology \mathcal{QC}_1) and `ibmq_lima` (Falcon r4T topology \mathcal{QC}_2). The topology of the device determines the possible placement of the two-qubit gates. The qubits are furthermore prone to decoherence, thereby requiring several runs of the experiment to make up for statistical errors. We measure the LZ, and concomitant KZM relation, for each one of the IBM-Q transmons in \mathcal{QC}_1 and \mathcal{QC}_2 . Each transmon plays the role of a quantum qubit, evolving with its own dynamics, experimentally showing the effects of decoherence on the hardware. Generally, the physical transmon type qubits of the same machine offer a variety of properties that describe the quality of the qubit, such as thermal relaxation time (T_1), dephasing time (T_2), anharmonicity, and error properties detailed in Appendix B, allowing us to compare the simulation's performance with different physical parameters. In Fig. 2, the times T_1 and T_2 are depicted for each considered circuit topology at two different dates, illustrating in a graphical way how these times change every time that IBM performed a calibration of every device.

The source code used for data acquisition is open and accessible through project repository [56].

IV. RESULTS

A. Simulation of the Landau-Zener evolution on IBM-Q

Unitary dynamics.- We are interested in the experimental determination, and its respective simulation, on a digital open-access IBM-Q of a single qubit evolution under a linearly time-dependent Hamiltonian (LZ problem). At time t_i , a qubit in the processor is initialized in the state $|\psi(t_i)\rangle = \hat{U}_n(\theta)|0\rangle$, where $\hat{U}_n(\theta) = \cos[\theta/2]\hat{I} - i\hat{\sigma}_n \sin[\theta/2]$ is a unitary rotation along the axis $n \in \{x, y, z\}$ with $\hat{\sigma}_n$ the usual Pauli matrix along the n -direction. The whole evolution from t_i to t_f is performed by sampling the Hamiltonian at regular intervals $dt = (t_f - t_i)/N_t$ where N_t denotes the number of time steps or the total circuit depth (see blue region in Fig.3(a)). The equivalent circuit for the experimental IBM-Q realization, and its simulation, is shown in Figure 3(a). Assuming an evolution governed by a time-independent Hamiltonian for small enough intervals of duration dt , the time evolution operator at time $t = N dt$ can be approximated by:

$$\hat{U}(t, t_i) \approx \prod_{k=0}^{N-1} e^{-i\hat{H}_k dt}. \quad (10)$$

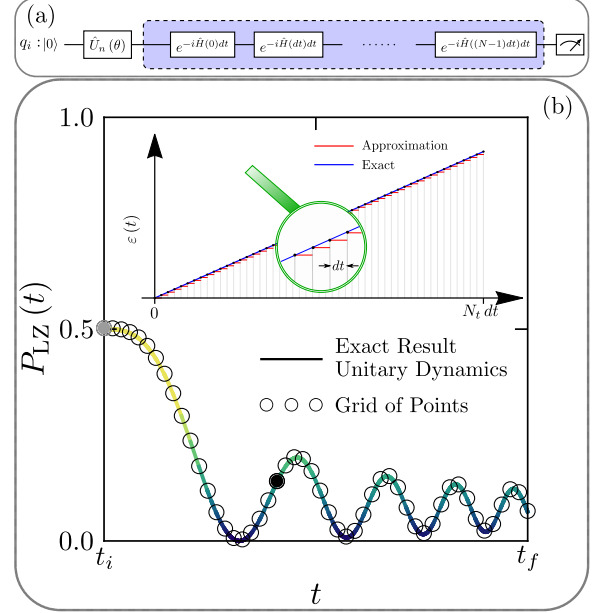


Figure 3. **IBM-Q circuit simulation of the Landau-Zener process.** (a) Quantum circuit for the LZ simulation starting at the state $|\psi(t_i)\rangle = \hat{U}_n(\theta)|0\rangle$, where $\hat{U}_n(\theta)$ is an unitary rotation along the axis n . (b) Schematic representation of the LZ transition probability: the solid line corresponds to the exact result given by Eq. (12), with $\Delta = 1$, $t_a = 2$, $t_i = 0$ and $t_f = 10$, while the symbols illustrate expected results for a grid of points with separation $dt = t_f - t_i/N_t$, being N_t the total circuit depth. The filled dots correspond to: the shortest circuit with depth 1 (gray dot) and an intermediate circuit depth N (black dot). The inset shows the discrete approximation of the time-dependent component $\varepsilon(t)$ of the LZ Hamiltonian.

where $\hat{H}_k = \hat{H}(t_i + kdt)$.

As we are interested in the evolution from an initial condition where the LZ system is prepared in an equal weight superposition at the anticrossing point, we start applying the unitary rotation $\hat{U}_y(-\pi/2)$. The approximate time evolution operator is constructed with general unitary gates. A general unitary single qubit gate describes rotations on the Bloch sphere and is defined by three Euler angles

$$\hat{U}(\theta, \phi, \lambda) = \begin{pmatrix} \cos\left(\frac{\theta}{2}\right) & -e^{i\lambda} \sin\left(\frac{\theta}{2}\right) \\ e^{i\phi} \sin\left(\frac{\theta}{2}\right) & e^{i(\phi+\lambda)} \sin\left(\frac{\theta}{2}\right) \end{pmatrix}. \quad (11)$$

The general unitary can then be expressed using the set $\{CX, I, U_z, \sqrt{X}, X\}$ of gates as $U(\theta, \phi, \lambda) = e^{i\gamma}\hat{U}_z(\phi + \pi)\sqrt{X}\hat{U}_z(\theta + \pi)\sqrt{X}\hat{U}_z(\lambda)$, where $\gamma = (\lambda + \phi + \pi)/2$ is a global phase factor. Using this decomposition, small time progressions as defined in Eq. (10) will be simulated and finally the state $|\psi(t)\rangle$ is measured.

As already stated, the Landau-Zener dynamics can be exactly solved (see Appendix A), thus allowing a direct

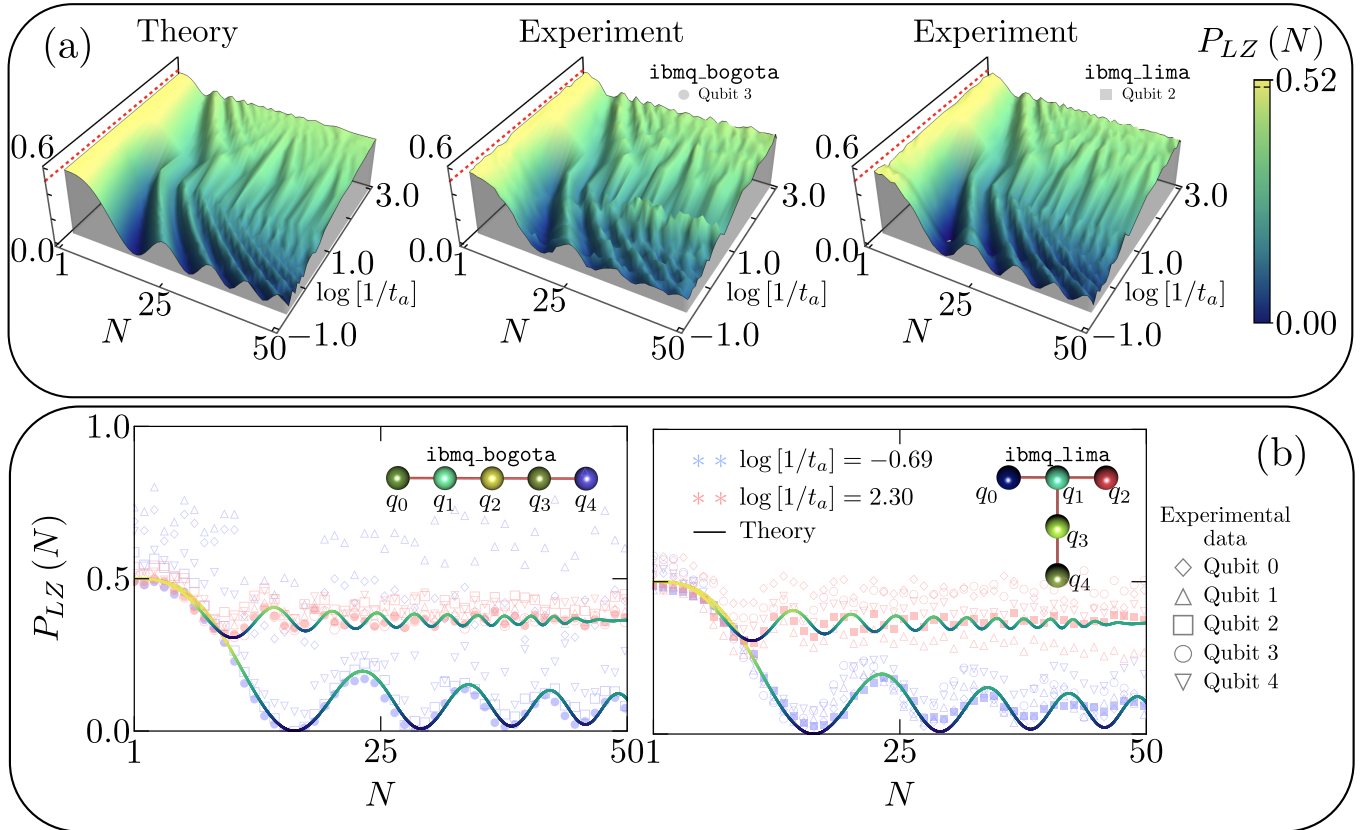


Figure 4. **Measurement of LZ probabilities on IBM-Q.** In panel (a), we establish a contrast between the exact and experimental results for the LZ probability transition as a function the number of layers or circuit depth N , and the annealing time t_a . In this panel, all figures share the same color vertical scale. The initial condition, $P_{\text{LZ}}(t=0) = 0.5$, is represented by a red dashed line. Note that in some region of parameters a probability larger than 0.5 for the experimental results is obtained. In panel (b), the behavior of the LZ probability for every qubit available in each processor is shown, identifying in this way the more isolated (larger decoherence time) qubit in each case. We fixed the maximum number of layers in the circuit as $N_t = 50$.

benchmark test of the experimental results on a realistic quantum device against exact results. For a LZ evolution starting at the anticrossing ground state, we obtain the LZ transition probability $P_{\text{LZ}}(t)$ at time t given as:

$$P_{\text{LZ}}(t) = |\chi_1 \mathbf{D}_{-i\delta}(z) + \chi_2 \mathbf{D}_{-1+i\delta}(iz)|^2. \quad (12)$$

with the amplitudes χ_1 and χ_2 , see Eq. (5), given by:

$$\begin{aligned} \chi_1 &= -\frac{2^k \exp[i\pi k]}{4\sqrt{ik}} \left[\frac{\sqrt{2ik}\Gamma(k) + (1+i)\Gamma(\frac{1}{2}+k)}{\Gamma(2k)} \right], \\ \chi_2 &= \frac{\exp[i\pi k]}{2^{k+1}} \left[\frac{2ik\Gamma(\frac{1}{2}-k) + (1-i)\sqrt{2ik}\Gamma(1-k)}{\Gamma(1-2k)} \right]. \end{aligned}$$

where z and δ are given in Sec. II B.

Our first aim is to benchmark our LZ experimental results with the above exact theoretical prediction. This is schematically illustrated in Fig. 3(b) where we display the exact result, see Eq. (12), and a hypothetical grid of points representing expected target data with a separation $dt = t_f - t_i/N_t$, being N_t the total circuit depth. For every experimental data, 5000 shots have

been realized on each quantum circuit, \mathcal{QC}_1 and \mathcal{QC}_2 .

The unity of energy is set by choosing $\Delta = 1$ in the LZ Hamiltonian (see Eq. (3)). Therefore, in the following, we express energy parameters and time as dimensionless quantities ($\hbar = 1$). Using the quantum circuits \mathcal{QC}_1 and \mathcal{QC}_2 , we implemented the corresponding gates in all qubits available on parallel and we did a sweep of parameters in annealing time t_a from 0.05 to 2.0. Additionally, for both theoretical and experimental results, the final evolution time t_f was chosen according with: $t_f = 4$ for annealing times in the interval $0.05 \leq t_a \leq 0.17$ and $t_f = 10$ for $0.17 < t_a \leq 2$. These particular choices have been supported by the fact that as we are mainly interested in the asymptotic LZ probability transition, a good asymptotic collapse is reached for these parameter regimes. Additionally, we also represent the experimental results $P_{\text{LZ}}(N)$ as a function of the number of layers in the circuit instead of time. We emphasize that a N -deep circuit corresponds to a physical qubit interaction time $t_{\text{Int}} = 2t_{SX}N$, where t_{SX} is the gate length property for \sqrt{X} and it

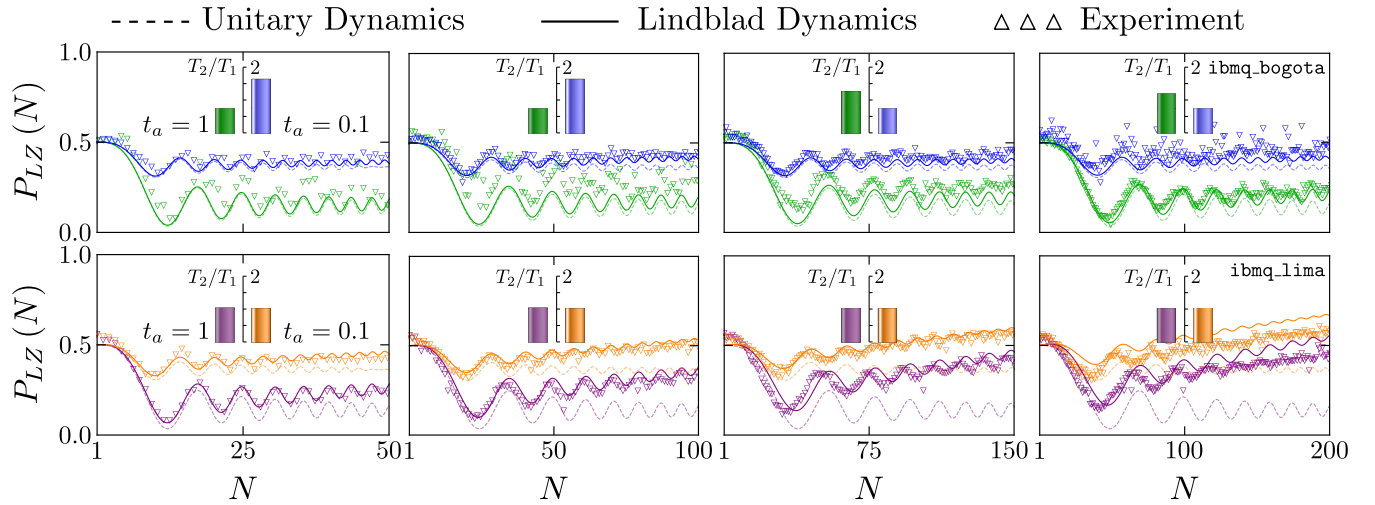


Figure 5. Contrast between close and open quantum dynamics for LZ on IBM-Q. The Landau-Zener transition probability is shown as a function of the number of layers N in the circuit implementation for qubit 4, the noisiest qubit for each \mathcal{QC}_1 and \mathcal{QC}_2 quantum circuit. We contrast the theoretical prediction for a close system (unitary dynamics) given by Eq. (12) (dashed line), the decoherent dynamics given by the numerical solution of the Lindblad equation (Eq. (13), solid line) and experimental results (symbols). The experimental results clearly depart from the unitary evolution prediction as the number of layers N_t increases in the circuit (see Fig. 3 blue region). Additionally, in every panel, we present as inset the ratio between the dephasing time (T_2) and the thermal relaxation time (T_1).

is fixed by IBM-Q as $t_{SX} = 35.555\text{ns}$. In Fig. 4, we present a contrast of the LZ probability transition for both the theoretical and experimental results. In the panel Fig. 4(a), we choose the most robust qubit that better reproduced the theoretical P_{LZ} . Specifically, we found that the qubit 3 and 2 for `ibmq_bogota` and `ibmq_lima` respectively, have the best performance. In order to appreciate better the experimental agreement and differences for every single-qubit over \mathcal{QC}_1 and \mathcal{QC}_2 , we show the LZ probability transition as a function of the physical interaction time in Fig. 4(b).

In the next sub-section, we address the influence of the number of layers in the LZ simulation circuit and the role of decoherence.

Open system dynamics.— The performance of the hardware worsens with an increasing depth of the circuit. The assumption of a closed quantum system rapidly breaks down for qubits with short relaxation (T_1) and dephasing (T_2) timescales, thus requiring for a theoretical analysis that resort to a quantum open system approach. The effects of quantum decoherence are noticeable in the measured probability when scaling the number of gates due to the increase in computing times. We model every qubit on IBM-Q as a two-level system coupled to a Markovian bath. The system evolution is described by a continuous map $\rho_t = e^{t\mathcal{L}}$, $t \geq 0$ generated by the Lindbladian [57]

$$\mathcal{L}[\bullet] = -i \left[\hat{H}, \bullet \right] + \sum_n \left(\hat{L}_n^\dagger \bullet \hat{L}_n - \frac{1}{2} \left\{ \hat{L}_n^\dagger \hat{L}_n, \bullet \right\} \right). \quad (13)$$

where, \hat{H} is the Hamiltonian and $\{\hat{L}_n\}$ are the Lindblad operators that describe the system-bath interactions. Dissipative processes in a superconducting qubit such as relaxation, i.e., transitions from the higher energy level $|1\rangle$ to ground state $|0\rangle$, can be described phenomenologically by the operator $\hat{L}_1 = \sqrt{\Gamma}|0\rangle\langle 1|$ and dephasing by rotations around the z axis $\hat{L}_2 = \sqrt{\gamma/2}\hat{\sigma}_z$. Additional transitions such as thermal excitations from the ground state $|0\rangle$ to $|1\rangle$ may also be considered [58], although for a superconducting transmon qubit this process is negligible. The rates $\Gamma = 1/T_1$ and $\gamma = 1/T_2$ are related to the characteristic times of each physical qubit.

QuTiP is an open-source framework for Python that allows for numerical simulations of quantum dynamics of open systems under different solvers [59, 60]. In Fig. 5, we establish a contrast between the unitary exact dynamics, numerical Lindblad dynamics, and the experimental results obtained for qubit 4, the noisiest qubit in both quantum machines. Specifically, we depicted the Landau-Zener probability as a function of the number of layers in the circuit, N , for two specific annealing times $t_a = 1$ (colors green/purple) and $t_a = 0.1$ (colors blue/orange). Additionally, we show as an inset the ratio T_2/T_1 , the bar scale show the value of this proportion from 0 to 2. Although, `ibmq_lima` quantum computer has the ratio T_2/T_1 almost constant the qubit 4 is the more prone to decoherence.

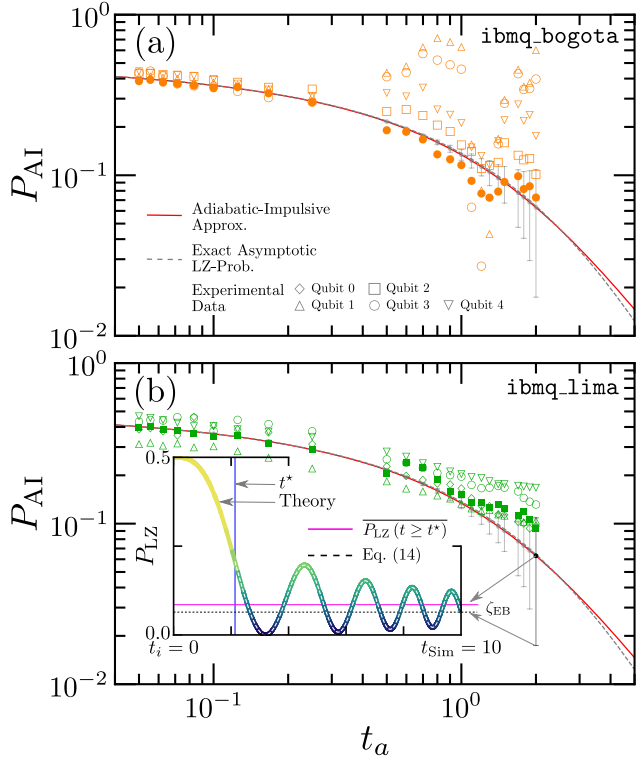


Figure 6. Simulation of the Kibble-Zurek mechanism on IBM-Q. In both upper and lower panels, we contrast the adiabatic-impulsive approximation (Eq. (8)), asymptotic Landau-Zener probability (Eq. (14)), and the experimental data. In panel (a), we show the experimental data retrieved from `ibmq_bogota`. In panel (b), we present the experimental results for `ibmq_lima`. In the inset, we present the protocol to calculate the asymptotic experimental Landau-Zener probability. The error bars with length $2\zeta_{EB}$, calculated from the finite-time effect, are also shown. Solid symbols are consistent with the best qubit behavior as depicted in Fig. 4.

B. Simulation of the Kibble-Zurek mechanism on IBM-Q

The main purpose of this work is to validate the adiabatic-impulsive approximation of the Kibble-Zurek mechanism through the nonequilibrium dynamics of the Landau-Zener model on IBM-Q. Using Eq.(12) with $\Delta = 1$, the asymptotic probability can be exactly calculated as:

$$P_{LZ}(t \rightarrow \infty) = 1 - \frac{1}{\delta} \exp \left[-\frac{3\pi\delta}{2} \right] |\chi_2|^2. \quad (14)$$

Expanding the asymptotic probability into series, we obtain

$$P_{LZ}(t \rightarrow \infty) = \frac{1}{2} - \frac{\sqrt{\pi}}{4} t_a^{1/2} + \frac{\sqrt{\pi}}{32} (\pi - \ln(4)) t_a^{3/2} + \mathcal{O}(t_a^{5/2}). \quad (15)$$

We find the value by directly comparing the adiabatic-impulsive approximation given by Eq. (9) and the expansion of the LZ asymptotic probability at the first order of

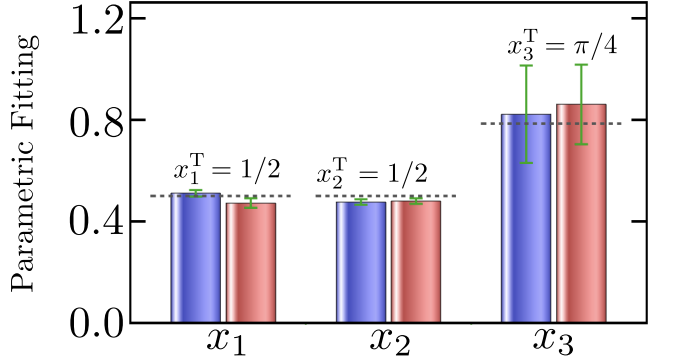


Figure 7. KZM adiabatic-impulsive approximation fitting parameters. From the best qubit experimental data (solid symbols in Fig. 6), the fitting to the KZM adiabatic-impulsive approximation $P_{AI}(t_a)$ given by Eq.(17) is probed (the dashed gray lines correspond to the theoretical predictions). The experimental data at `ibmq_bogota` and `ibmq_lima` are depicted in blue and red, respectively.

$\eta = \pi/4$. However, non-trivial corrections for high-order terms appear. In both main panels of Figs. 6(a-b), we depict the agreement of the theoretical prediction for the adiabatic-impulsive approximation (Eq. (8)) and asymptotic Landau-Zener probability (Eq. (14)). We note the role of the corrections for large quench times. For finite-time LZ simulations, estimating the asymptotic probability transition becomes challenging and similar to experimental data. To this end, we introduced the Landau-Zener jump-time t^* as the first zero in the second derivative of the Landau-Zener probability, thus:

$$\left. \frac{d^2 P_{LZ}(t)}{dt^2} \right|_{t=t^*} = 0. \quad (16)$$

In this way, we propose that the estimated finite-time asymptotic Landau-Zener probability can be approximated by the average of all values of $P_{LZ}(t)$ with $t \geq t^*$. In the inset of Fig. 6(b), we display the protocol implemented to calculate the finite-time asymptotic Landau-Zener probability. Therefore, we establish a finite-time error regime depicted in the main panel of Figs. 6(a-b) as error bars using the experimental values of the annealing time. The estimation of the Landau-Zener jump-time t^* has been implemented uniquely from the theoretical prediction, assuming it will be the same for the experimental data. Note that the adiabatic-impulsive approximation and the asymptotic Landau-Zener probability are equivalent in the regime of our experimental data giving confidence in our validation of the KZM in the IBM-Q platforms.

For the qubit with the largest decoherence T_1 and T_2 times (the best qubit from now on), the experimental data show an excellent agreement with the theoretical predictions for the impulsive-adiabatic approximation.

For large annealing time t_a , the experimental data has a significant deviation for some qubits in the `ibmq_bogota` quantum computer. Indeed, the adiabatic-impulsive approximation relationship with the Landau-Zener problem assumes a close system's quantum dynamics. However, since IBM-Q is benchmarked as an open-quantum system, deviations are to be expected.

In order to further testing the KZM adiabatic-impulse approximation, from our experimental data, we rewrite the Eq. (8) in terms of 3 fitting parameters, as:

$$P_{AI}(t_a) \simeq x_1 - x_2 \sqrt{1 - \frac{2}{(x_3 t_a)^2 + x_3 t_a \sqrt{(x_3 t_a)^2 + 4} + 2}}. \quad (17)$$

In Fig. (7), we depict the comparison of the fitting parameters x_1 , x_2 and x_3 for the best qubit at `ibmq_bogota` and `ibmq_lima`. The structure of the fitting expression allows us a direct comparison with the theoretical predictions (x_1^T, x_2^T, x_3^T) . The first fitting parameter x_1 provides information about how robust the qubit is to decoherence for fast LZ driving. Note that the theoretical prediction is $x_1^T = 1/2$ as it is fixed by the initial condition at the anticrossing initial point. Moreover, it fixes the value of the impulsive-adiabatic approximation for small annealing times, $P_{AI}(t_a \rightarrow 0) = 1/2$. It is evident from Fig. 6 that some qubits deviate from this ideal value in this regime, confirming that these qubits are already highly sensible to decoherence. Nonetheless, for these results, we used the smallest number of layers considered. The second fitting parameter x_2 gives information about the higher annealing time regime. The asymptotic value of the adiabatic-impulsive approximation is zero for large annealing times. However, large annealing times imply that the LZ transition probability has several oscillations as a function of time. As a consequence, it is necessary to manage large simulation times to obtain the asymptotic LZ probability. It is to be expected that, our results show deviations due to finite simulation time effects. Finally, the third parameter x_3 validates the Kibble-Zurek scaling in the adiabatic-impulsive approximation. We found an excellent agreement with the theoretical predictions for these QC_1 and QC_2 robust qubits.

V. CONCLUSIONS

In this work we explored the dynamics of a two level system under the time-dependent Landau-Zener Hamiltonian on digital IBM Quantum computers. Time evolution was simulated by discretization of the time dependent Hamiltonian and application of subsequent single-qubit unitary gates representing finite time progressions. We studied the Landau Zener transition probability as a function of time by running parallel quantum circuits on 5-qubit machines `ibmq_lima` and `ibmq_bogota` with different topologies. We find a strong agreement with the theoretical solution of the

LZ problem for robust qubits from both machines. We also considered the effect of decoherence on an open LZ system, modeling the dissipation using collapse operators for relaxation and dephasing. For greater Trotterizations of the time evolution operator, increasing computing time cause noticeable deviations from the ideal LZ solution. The numerical solution of the Lindblad master equation accurately depicts the open system's relaxation towards the ground state, supported by the measured probabilities.

The above positive LZ results allowed us to demonstrate the first simulation on a realistic quantum computer of the universal Kibble-Zurek mechanism by estimating the asymptotic transition probability obtained from LZ experimental data. Results show excellent agreement for the best qubits considered in each device and low annealing times. We find that larger annealing times demand a greater time resolution in the evolution operator discretization, putting practical limits on the performance achieved, as it becomes limited by the conflict between computing depth and decoherence times. However, the rapid rate of quantum hardware progress may soon change this. Furthermore, an interesting follow-up research direction would consist in focusing on richer open quantum platforms, where KZM has been poorly explored. Thus, using real quantum hardware to test quantum universal dynamical behaviors, in both closed and open systems, represent an interesting extension of the results presented in this work.

VI. ACKNOWLEDGMENTS

F.J.G-R acknowledges financial support from European Commission FET-Open project AVaQus GA 899561. S.H-Q, F.J.R. and L.Q. are thankful for the financial support from Facultad de Ciencias-UniAndes project “*Dinámica de bits cuánticos (qubits) fijos y móviles: Eco de Loschmidt*” (2022-2023).

Appendix A: LZ Formal Solution

Here, we present a way to calculate the LZSM transition probability depending on the initial conditions. Consider the time-dependent Schrödinger equation

$$i \frac{d}{dt} |\psi(t)\rangle = \hat{H}(t) |\psi(t)\rangle. \quad (A1)$$

Where, the Hamiltonian $\hat{H}(t)$ is given by Eq. (3). We write the wave function as a linear combination of diabatic states given by

$$|\psi(t)\rangle = \alpha(t)|0\rangle + \beta(t)|1\rangle. \quad (A2)$$

In general, we consider the time-evolution from an initial time t_i to a final time t_f . Therefore, the wavefunction initial condition is fixed by $|\psi(t_i)\rangle = \alpha_i|0\rangle +$

$\beta_i |1\rangle$. The probability amplitudes α_i and β_i satisfies that $|\alpha_i|^2 + |\beta_i|^2 = 1$. By direct substitution of Eq. (A2) into Eq. (A1), we obtain the system of differential equations

$$i \frac{d}{dt} \alpha(t) = -\frac{\varepsilon(t)}{2} \alpha(t) - \frac{\Delta}{2} \beta(t), \quad (\text{A3a})$$

$$i \frac{d}{dt} \beta(t) = -\frac{\Delta}{2} \alpha(t) + \frac{\varepsilon(t)}{2} \beta(t). \quad (\text{A3b})$$

Decoupling the differential equations, we obtain

$$\begin{aligned} \frac{d^2 \alpha(t)}{dt^2} &= - \left[\left(\frac{\varepsilon(t)}{2} \right)^2 + \left(\frac{\Delta}{2} \right)^2 + \frac{i}{2} \frac{d\varepsilon(t)}{dt} \right] \alpha(t), \\ \frac{d^2 \beta(t)}{dt^2} &= - \left[\left(\frac{\varepsilon(t)}{2} \right)^2 + \left(\frac{\Delta}{2} \right)^2 - \frac{i}{2} \frac{d\varepsilon(t)}{dt} \right] \beta(t). \end{aligned} \quad (\text{A4})$$

Using the linear bias $\varepsilon(t)$ dependence and the substitution $t = \sqrt{2t_a}\tau$, we rewrote the previous differential equations in the form of two parabolic cylinder differential equation:

$$\frac{d^2}{d\tau^2} \alpha(\tau) + (2\delta + i + \tau^2) \alpha(\tau) = 0. \quad (\text{A5a})$$

$$\frac{d^2}{d\tau^2} \beta(\tau) + (2\delta - i + \tau^2) \beta(\tau) = 0, \quad (\text{A5b})$$

Where, we defined $\delta = \Delta^2 t_a / 4$ as the adiabaticity parameter. The canonical form of the parabolic cylinder differential equation is the second-order ordinary differential equation

$$\frac{d^2}{dz^2} u(z) + \left(p + \frac{1}{2} - \frac{z^2}{4} \right) u(z) = 0, \quad (\text{A6})$$

whose solution is given by

$$u(z) = c_1 \mathbf{D}_p(z) + c_2 \mathbf{D}_{-p-1}(iz), \quad (\text{A7})$$

where $\mathbf{D}_p(z)$ is a parabolic cylinder function and the constants c_1 (c_2) depend on the initial conditions [61]. Additionally, The Weber's equation (Eq. (A6)) has a symmetry by simultaneously replace p and z by $-p-1$ and $\pm iz$ respectively [62]. Therefore, $\mathbf{D}_p(-z)$, $\mathbf{D}_{-p-1}(-iz)$ are solutions of Weber's equation. These four solutions are linearly dependent [63]. We transform the Eq.(A5a) and Eq.(A5b) in the form of Eq. (A6) using the substitution $z = \sqrt{2}\tau \exp[i\pi/4]$. We obtained

$$\frac{d^2}{dz^2} \alpha(z) + \left(-i\delta - \frac{1}{2} - \frac{z^2}{4} \right) \alpha(z) = 0, \quad (\text{A8a})$$

$$\frac{d^2}{dz^2} \beta(z) + \left(-i\delta + \frac{1}{2} - \frac{z^2}{4} \right) \beta(z) = 0. \quad (\text{A8b})$$

We propose a formal solution of Eq. (A8b) given by

$$\beta(z) = \chi_1 \mathbf{D}_{-i\delta}(z) + \chi_2 \mathbf{D}_{-1+i\delta}(iz). \quad (\text{A9})$$

Where, χ_1 and χ_2 are the initial conditions at $z = z_i$. On the other hand, we rewrote Eq. (A3b) as

$$\alpha(z) = \frac{e^{-i\frac{\pi}{4}}}{\sqrt{\delta}} \left[\frac{d}{dz} \beta(z) + \frac{1}{2} z \beta(z) \right]. \quad (\text{A10})$$

By direct substitution of Eq. (A9) into Eq. (A10), and using the recurrence formulae given by

$$\mathbf{D}_{n+1}(z) - z \mathbf{D}_n(z) + n \mathbf{D}_{n-1}(z) = 0 \quad (\text{A11a})$$

$$\mathbf{D}'_n(z) + \frac{1}{2} z \mathbf{D}_n(z) - n \mathbf{D}_{n-1}(z) = 0, \quad (\text{A11b})$$

we obtain

$$\alpha(z) = \frac{e^{-i\frac{3\pi}{4}}}{\sqrt{\delta}} [\delta \chi_1 \mathbf{D}_{-1-i\delta}(z) + \chi_2 \mathbf{D}_{i\delta}(iz)]. \quad (\text{A12})$$

Now, we can find χ_1 and χ_2 from the initial conditions at $z = z_i$ with certain $\alpha(z_i)$ and $\beta(z_i)$:

$$\chi_1 = \frac{e^{i\frac{3\pi}{4}} \sqrt{\delta} \mathbf{D}_{-1+i\delta}(iz_i) \alpha(z_i) - \mathbf{D}_{i\delta}(iz_i) \beta(z_i)}{\delta \mathbf{D}_{-1-i\delta}(z_i) \mathbf{D}_{-1+i\delta}(iz_i) - \mathbf{D}_{-i\delta}(z_i) \mathbf{D}_{i\delta}(iz_i)}, \quad (\text{A13})$$

$$\chi_2 = \frac{-e^{i\frac{3\pi}{4}} \sqrt{\delta} \mathbf{D}_{-i\delta}(z_i) \alpha(z_i) + \delta \mathbf{D}_{-1-i\delta}(z_i) \beta(z_i)}{\delta \mathbf{D}_{-1-i\delta}(z_i) \mathbf{D}_{-1+i\delta}(iz_i) - \mathbf{D}_{-i\delta}(z_i) \mathbf{D}_{i\delta}(iz_i)}. \quad (\text{A14})$$

1. Exact solution of LZ evolution starting at the anticrossing state

We are interested in the evolution when the system is in the ground state at $t = 0$. The state is given by $|\psi(0)\rangle = (|0\rangle - |1\rangle)/\sqrt{2}$. Therefore, $\alpha(z_i) = 1/\sqrt{2}$ and $\beta(z_i) = -1/\sqrt{2}$. Additionally, we can express z as function of t as $z = \frac{t}{\sqrt{t_a}} \exp[i\pi/4]$. Therefore, we evaluate the following limits

$$\lim_{z_i \rightarrow 0} \mathbf{D}_n(\pm z_i) = \lim_{z_i \rightarrow 0} \mathbf{D}_n(\pm iz_i) = \frac{2^{n/2} \sqrt{\pi}}{\Gamma(\frac{1-n}{2})}, \quad (\text{A15})$$

$$\lim_{z_i \rightarrow 0} [\delta \mathbf{D}_{-1-i\delta}(z_i) \mathbf{D}_{-1+i\delta}(iz_i) - \mathbf{D}_{-i\delta}(z_i) \mathbf{D}_{i\delta}(iz_i)] = -\exp[-i\pi k], \quad \text{with } k = -\frac{i\delta}{2}. \quad (\text{A16})$$

Therefore, we obtain the values of χ_1 and χ_2 as:

$$\begin{aligned} \chi_1 &= -\frac{2^k \exp[i\pi k]}{4\sqrt{i\bar{k}}} \left[\frac{\sqrt{2i\bar{k}}\Gamma(k) + (1+i)\Gamma(\frac{1}{2}+k)}{\Gamma(2k)} \right], \\ \chi_2 &= \frac{\exp[i\pi k]}{2^{k+1}} \left[\frac{2ik\Gamma(\frac{1}{2}-k) + (1-i)\sqrt{2i\bar{k}}\Gamma(1-k)}{\Gamma(1-2k)} \right]. \end{aligned}$$

Here, we used the following Gamma-function relations

$$2^{2z-1}\Gamma(z)\Gamma\left(\frac{1}{2}+z\right) = \sqrt{\pi}\Gamma(2z), \quad (\text{A17})$$

$$\Gamma(1-z) = -z\Gamma(-z). \quad (\text{A18})$$

Now we calculate the asymptotic transition probability to the higher energy eigenstate

$$|\langle 1|\psi(t \rightarrow \infty) \rangle|^2 = 1 - |\alpha(t \rightarrow \infty)|^2, \quad (\text{A19})$$

using the expansions for parabolic cylinder functions [63]

$$\mathbf{D}_p(z) \sim e^{-z^2/4}z^p - \frac{\sqrt{2\pi}}{\Gamma(-p)}e^{i\pi p}e^{z^2/4}z^{-p-1} \quad \text{for } \frac{\pi}{4} < \arg(z) < \frac{5\pi}{4}, \quad (\text{A20})$$

$$\mathbf{D}_p(z) \sim e^{-z^2/4}z^p \quad \text{for } |\arg(z)| < \frac{3\pi}{4}. \quad (\text{A21})$$

whenever $|z| \rightarrow \infty$. We obtain the limiting values for the relevant parabolic cylinder functions

$$\mathbf{D}_{-1-i\delta}(z|_{t \rightarrow \infty}) = 0, \quad (\text{A22})$$

$$\mathbf{D}_{i\delta}(iz|_{t \rightarrow \infty}) = e^{-\frac{3\pi\delta}{4} + i\phi(t)}, \quad (\text{A23})$$

where $\phi(t) = t^2/4t_a + \delta \log(t/\sqrt{t_a})$ is a time dependent phase. By substitution into Eq. (A12) and (A19), we obtain the asymptotic transition probability

$$P_{\text{LZ}}(t \rightarrow \infty) = 1 - \frac{e^{-\frac{3\pi\delta}{2}}}{\delta} |\chi_2|^2. \quad (\text{A24})$$

2. Exact solution of LZ evolution starting from the ground state

In the classical LZ problem, evolution starts from the ground state $|0\rangle$ of the LZ Hamiltonian at $t = -\infty$. Then, we may set $\alpha(-\infty) = 1$ and $\beta(-\infty) = 0$ as initial conditions. Using the asymptotic expansions Eq. (A20) and (A21) and substitution into relations (A13) and (A14), we determine the coefficients corresponding to the classical LZ problem initial conditions

$$\chi_1 = 0, \quad (\text{A25})$$

$$\chi_2 = \sqrt{\delta}e^{-\pi\delta/4}. \quad (\text{A26})$$

Given this result, the transition probabilities can be written compactly as

$$|\langle 0|\psi(z) \rangle|^2 = e^{-\pi\delta/2} |\mathbf{D}_{i\delta}(iz)|^2, \quad (\text{A27})$$

$$|\langle 1|\psi(z) \rangle|^2 = \delta e^{-\pi\delta/2} |\mathbf{D}_{-1+i\delta}(iz)|^2, \quad (\text{A28})$$

and the classical LZ formula can directly recovered by applying the asymptotic expansion (A21) on Eq. (A27), where we obtain

$$P_{\text{LZ}} = e^{-2\pi\delta}. \quad (\text{A29})$$

Appendix B: Systematic Readout Error Mitigation

Results obtained from the available quantum hardware are subject to multiple sources of error including thermal relaxation, gate errors and faulty readout of the prepared quantum state [64]. A common first order approach to mitigate systematic readout errors is through a qubit's calibration matrix. For a single qubit this is defined to be

$$\mathbf{A} = \begin{pmatrix} p_{00} & p_{01} \\ p_{10} & p_{11} \end{pmatrix}, \quad (\text{B1})$$

where p_{ij} are the probabilities that a qubit prepared in state $|j\rangle$ is measured in state $|i\rangle$, for an ideal quantum computer this would be equal to the identity matrix. For a particular qubit of an IBM Quantum Computer, the calibration matrix can be found from the computer's system properties. Properties `prob_meas1_prep0`

and prob_meas0_prep1 correspond to p_{10} and p_{01} respectively. The diagonal terms of the calibration matrix can then be determined as the sum of elements in the columns must be equal to 1.

Systematic errors for a great number of executions can then be mitigated by inversion of the calibration matrix since $\vec{P}_{\text{noisy}} = \mathbf{A} \vec{P}_{\text{ideal}}$. Thus a useful calibration formula

to infer the ideal results is

$$\vec{P}_{\text{ideal}} = \mathbf{A}^{-1} \vec{P}_{\text{noisy}}, \quad (\text{B2})$$

where $\vec{P}_{\text{noisy}} = [P_0, P_1]^T$ is the vector of experimental probabilities P_i of the measured quantum state.

[1] J. Preskill, Quantum Computing in the NISQ era and beyond, *Quantum* **2**, 79 (2018).

[2] K. Bharti, A. Cervera-Lierta, T. H. Kyaw, T. Haug, S. Alperin-Lea, A. Anand, M. Degroote, H. Heimonen, J. S. Kottmann, T. Menke, W.-K. Mok, S. Sim, L.-C. Kwek, and A. Aspuru-Guzik, Noisy intermediate-scale quantum algorithms, *Rev. Mod. Phys.* **94**, 015004 (2022).

[3] F. Arute, K. Arya, R. Babbush, and *et al*, Quantum supremacy using a programmable superconducting processor, *Nature* **574**, 505 (2019).

[4] H.-S. Zhong, H. Wang, Y.-H. Deng, M.-C. Chen, L.-C. Peng, Y.-H. Luo, J. Qin, D. Wu, X. Ding, Y. Hu, P. Hu, X.-Y. Yang, W.-J. Zhang, H. Li, Y. Li, X. Jiang, L. Gan, G. Yang, L. You, Z. Wang, L. Li, N.-L. Liu, C.-Y. Lu, and J.-W. Pan, Quantum computational advantage using photons, *Science* **370**, 1460 (2020).

[5] G. J. Mooney, G. A. L. White, C. D. Hill, and L. C. L. Hollenberg, Whole-device entanglement in a 65-qubit superconducting quantum computer, *Advanced Quantum Technologies* **4**, 2100061 (2021).

[6] S. T. Flammia and Y.-K. Liu, Direct fidelity estimation from few pauli measurements, *Phys. Rev. Lett.* **106**, 230501 (2011).

[7] M. P. da Silva, O. Landon-Cardinal, and D. Poulin, Practical characterization of quantum devices without tomography, *Phys. Rev. Lett.* **107**, 210404 (2011).

[8] T. J. Proctor, A. Carignan-Dugas, K. Rudinger, E. Nielsen, R. Blume-Kohout, and K. Young, Direct randomized benchmarking for multiqubit devices, *Phys. Rev. Lett.* **123**, 030503 (2019).

[9] IBM-Corporation, Quantum computing IBM, <https://quantum-computing.ibm.com> (2022), accessed: 2022-07-27.

[10] T. W. B. Kibble, Topology of cosmic domains and strings, *J. of Phys. A: Math. Gen.* **9**, 1387 (1976).

[11] T. W. B. Kibble, Some implications of a cosmological phase transition, *Phys. Reports* **67**, 183 (1980).

[12] W. H. Zurek, Cosmological experiments in superfluid helium?, *Nature* **317**, 505 (1985).

[13] W. H. Zurek, Cosmological experiments in condensed matter systems, *Phys. Reports* **276**, 177 (1993).

[14] W. H. Zurek, U. Dorner, and P. Zoller, Dynamics of a quantum phase transition, *Phys. Rev. Lett.* **95**, 105701 (2005).

[15] J. Dziarmaga, Dynamics of a quantum phase transition: Exact solution of the quantum Ising model, *Phys. Rev. Lett.* **95**, 245701 (2005).

[16] O. L. Acevedo, L. Quiroga, F. J. Rodríguez, and N. F. Johnson, New dynamical scaling universality for quantum networks across adiabatic quantum phase transitions, *Phys. Rev. Lett.* **112**, 030403 (2014).

[17] F. J. Gómez-Ruiz, J. J. Mayo, and A. del Campo, Full counting statistics of topological defects after crossing a phase transition, *Phys. Rev. Lett.* **124**, 240602 (2020).

[18] A. del Campo, Universal statistics of topological defects formed in a quantum phase transition, *Phys. Rev. Lett.* **121**, 200601 (2018).

[19] J. Goo, Y. Lim, and Y. Shin, Defect saturation in a rapidly quenched Bose gas, *Phys. Rev. Lett.* **127**, 115701 (2021).

[20] J.-M. Cui, F. J. Gómez-Ruiz, Y.-F. Huang, C.-F. Li, G.-C. Guo, and A. del Campo, Experimentally testing quantum critical dynamics beyond the Kibble-Zurek mechanism, *Communications Physics* **3**, 10.1038/s42005-020-0306-6 (2020).

[21] Y. Bando, Y. Susa, H. Oshiyama, N. Shibata, M. Ohzeki, F. J. Gómez-Ruiz, D. A. Lidar, S. Suzuki, A. del Campo, and H. Nishimori, Probing the universality of topological defect formation in a quantum annealer: Kibble-Zurek mechanism and beyond, *Phys. Rev. Research* **2**, 033369 (2020).

[22] A. D. King, S. Suzuki, J. Raymond, A. Zucca, T. Lanting, F. Altomare, A. J. Berkley, S. Ejtemaei, E. Hoskinson, S. Huang, E. Ladizinsky, A. MacDonald, G. Marsden, T. Oh, G. Poulin-Lamarre, M. Reis, C. Rich, Y. Sato, J. D. Whittaker, J. Yao, R. Harris, D. A. Lidar, H. Nishimori, and M. H. Amin, *Coherent quantum annealing in a programmable 2000-qubit ising chain* (2022).

[23] M. Anquez, B. A. Robbins, H. M. Bharath, M. Boguslawski, T. M. Hoang, and M. S. Chapman, Quantum Kibble-Zurek mechanism in a spin-1 Bose-Einstein condensate, *Phys. Rev. Lett.* **116**, 155301 (2016).

[24] A. Keesling, A. Omran, H. Levine, H. Bernien, H. Pichler, S. Choi, R. Samajdar, S. Schwartz, P. Silvi, S. Sachdev, P. Zoller, M. Endres, M. Greiner, V. Vuletić, and M. D. Lukin, Quantum Kibble-Zurek mechanism and critical dynamics on a programmable Rydberg simulator, *Nature* **568**, 207 (2019).

[25] L. Landau, Zur theorie der energieübertragung, *Phyz. Z. Sowjetunion* **1**, 88 (1932); Zur theorie der energieübertragung II, *2*, 46 (1932).

[26] C. Zener and R. H. Fowler, Non-adiabatic crossing of energy levels, *Proceedings of the Royal Society of London. Series A, Containing Papers of a Mathematical and Physical Character* **137**, 696 (1932).

[27] E. C. G. Stückelberg, Theory of inelastic collisions between atoms, *Helv. Phys. Acta* **5**, 369 (1932).

[28] E. Majorana, Atomi orientati in campo magnetico variabile, *Il Nuovo Cimento (1924-1942)* **43**, 50 (1932).

[29] B. Damski, The simplest quantum model supporting the Kibble-Zurek mechanism of topological defect production: Landau-Zener transitions from a new perspective, *Phys. Rev. Lett.* **95**, 035701 (2005).

[30] B. Damski and W. H. Zurek, Adiabatic-impulse approxi-

mation for avoided level crossings: From phase-transition dynamics to Landau-Zener evolutions and back again, *Phys. Rev. A* **73**, 063405 (2006).

[31] X.-Y. Xu, Y.-J. Han, K. Sun, J.-S. Xu, J.-S. Tang, C.-F. Li, and G.-C. Guo, Quantum simulation of Landau-Zener model dynamics supporting the Kibble-Zurek mechanism, *Phys. Rev. Lett.* **112**, 035701 (2014).

[32] M. Gong, X. Wen, G. Sun, D.-W. Zhang, D. Lan, Y. Zhou, Y. Fan, Y. Liu, X. Tan, H. Yu, Y. Yu, S.-L. Zhu, S. Han, and P. Wu, Simulating the Kibble-Zurek mechanism of the ising model with a superconducting qubit system, *Scientific Reports* **6**, 22667 (2016).

[33] L. Wang, C. Zhou, T. Tu, H.-W. Jiang, G.-P. Guo, and G.-C. Guo, Quantum simulation of the Kibble-Zurek mechanism using a semiconductor electron charge qubit, *Phys. Rev. A* **89**, 022337 (2014).

[34] J.-M. Cui, Y.-F. Huang, Z. Wang, D.-Y. Cao, J. Wang, W.-M. Lv, L. Luo, A. del Campo, Y.-J. Han, C.-F. Li, and G.-C. Guo, Experimental trapped-ion quantum simulation of the Kibble-Zurek dynamics in momentum space, *Scientific Reports* **6**, 101038/srep33381 (2016).

[35] S. Andersson and *et al*, Learn quantum computation using Qiskit (2020).

[36] G. Aleksandrowicz and *et al*, Qiskit: An open-source framework for quantum computing (2019).

[37] A. Cervera-Lierta, Exact Ising model simulation on a quantum computer, *Quantum* **2**, 114 (2018).

[38] M. Rodriguez-Vega, E. Carlander, A. Bahri, Z.-X. Lin, N. A. Sinitzyn, and G. A. Fiete, Real-time simulation of light-driven spin chains on quantum computers, *Physical Review Research* **4**, 10.1103/physrevresearch.4.013196 (2022).

[39] J. M. Koh, T. Tai, Y. H. Phee, W. E. Ng, and C. H. Lee, Stabilizing multiple topological fermions on a quantum computer, *npj Quantum Information* **8**, 10.1038/s41534-022-00527-1 (2022).

[40] M. B. Pozzobom and J. Maziero, Preparing tunable Bell-diagonal states on a quantum computer, *Quantum Information Processing* **18**, 10.1007/s11128-019-2264-z (2019).

[41] Y. Wang, Y. Li, Z. qi Yin, and B. Zeng, 16-qubit IBM universal quantum computer can be fully entangled, *NPJ Quantum Information* **4**, 10.1038/s41534-018-0095-x (2018).

[42] K. Choo, C. W. von Keyserlingk, N. Regnault, and T. Neupert, Measurement of the entanglement spectrum of a symmetry-protected topological state using the IBM quantum computer, *Physical Review Letters* **121**, 10.1103/physrevlett.121.086808 (2018).

[43] D. Cruz, R. Fournier, F. Gremion, A. Jeannerot, K. Komagata, T. Tasic, J. Thiesbrummel, C. L. Chan, N. Macris, M.-A. Dupertuis, and C. Javerzac-Galy, Efficient quantum algorithms for GHZ and W states, and implementation on the IBM quantum computer, *Advanced Quantum Technologies* **2**, 1900015 (2019).

[44] G. J. Mooney, C. D. Hill, and L. C. L. Hollenberg, Entanglement in a 20-qubit superconducting quantum computer, *Scientific Reports* **9**, 10.1038/s41598-019-49805-7 (2019).

[45] A. A. Zhukov, S. V. Remizov, W. V. Pogosov, and Y. E. Lozovik, Algorithmic simulation of far-from-equilibrium dynamics using quantum computer, *Quantum Information Processing* **17**, 10.1007/s11128-018-2002-y (2018).

[46] A. Solfanelli, A. Santini, and M. Campisi, Experimental verification of fluctuation relations with a quantum computer, *PRX Quantum* **2**, 030353 (2021).

[47] S. Gherardini, A. Belenchia, M. Paternostro, and A. Trombettoni, End-point measurement approach to assess quantum coherence in energy fluctuations, *Phys. Rev. A* **104**, L050203 (2021).

[48] G. García-Pérez, IBM Q experience as a versatile experimental testbed for simulating open quantum systems, *npj Quantum Information* **6**, 1 (2020).

[49] R. Puebla, O. Marty, and M. B. Plenio, Quantum Kibble-Zurek physics in long-range transverse-field Ising models, *Phys. Rev. A* **100**, 032115 (2019).

[50] R. Puebla, A. Smirne, S. F. Huelga, and M. B. Plenio, Universal anti-Kibble-Zurek scaling in fully connected systems, *Phys. Rev. Lett.* **124**, 230602 (2020).

[51] F. J. Gómez-Ruiz and A. del Campo, Universal dynamics of inhomogeneous quantum phase transitions: Suppressing defect formation, *Phys. Rev. Lett.* **122**, 080604 (2019).

[52] J. Dziarmaga and M. M. Rams, Dynamics of an inhomogeneous quantum phase transition, *New J. Phys.* **12**, 055007 (2010).

[53] M. Collura and D. Karevski, Critical quench dynamics in confined systems, *Phys. Rev. Lett.* **104**, 200601 (2010).

[54] D. Sen, K. Sengupta, and S. Mondal, Defect production in nonlinear quench across a quantum critical point, *Phys. Rev. Lett.* **101**, 016806 (2008).

[55] R. Barankov and A. Polkovnikov, Optimal nonlinear passage through a quantum critical point, *Phys. Rev. Lett.* **101**, 076801 (2008).

[56] S. Higuera-Quintero, F. J. Gómez-Ruiz, F. Rodríguez, and L. Quiroga, Repository for “Testing the Kibble-Zurek Mechanism Through a Digital Quantum Computer” (2021), this repository will be available at.

[57] H.-P. Breuer and F. Petruccione, *The Theory of Open Quantum Systems* (Oxford University Press, 2007).

[58] F. Marquardt and A. Püttmann, Introduction to dissipation and decoherence in quantum systems (2008), [arXiv:0809.4403](https://arxiv.org/abs/0809.4403).

[59] J. Johansson, P. Nation, and F. Nori, QuTiP: An open-source python framework for the dynamics of open quantum systems, *Computer Physics Communications* **183**, 1760 (2012).

[60] J. Johansson, P. Nation, and F. Nori, QuTiP 2: A python framework for the dynamics of open quantum systems, *Computer Physics Communications* **184**, 1234 (2013).

[61] H. Weber, Ueber die integration der partiellen differentialgleichung: $\frac{\partial^2 u}{\partial x^2} + \frac{\partial^2 u}{\partial y^2} + k^2 u = 0$., *Mathematische Annalen* **1**, 1 (1869).

[62] E. T. Whittaker and G. N. Watson, *A Course of Modern Analysis*, 5th ed., edited by V. H. Moll (Cambridge University Press, 2021).

[63] I. S. Gradshteyn, I. M. Ryzhik, D. Zwillinger, and V. Moll, *Table of integrals, series, and products*; 8th ed. (Academic Press, Amsterdam, 2014).

[64] D. Bultrini, M. Gordon, E. López, and G. Sierra, Simple mitigation strategy for a systematic gate error in IBMQ, *Journal of Applied Mathematics and Physics* **09**, 1215 (2021)